chemosensors

MDPI

*Article*

# Pd- and PdO-Decorated $TiO_2$ Nanospheres: Hydrogen Sensing Properties under Visible Light Conditions at Room Temperature

**Thilini Thathsara, Christopher J. Harrison, Rosalie K. Hocking and Mahnaz Shafiei ***

School of Science, Computing and Engineering Technologies, Swinburne University of Technology, Hawthorn, VIC 3122, Australia; tsarniakankanamge@swin.edu.au (T.T.); cjharrison@swin.edu.au (C.J.H.); rhocking@swin.edu.au (R.K.H.)

* Correspondence: mshafiei@swin.edu.au

**Abstract:** As a promising sustainable and clean energy source for the future, hydrogen plays an important role. Due to its high flammability and the explosive nature of hydrogen gas, it is crucial to employ reliable sensors that can detect the presence of hydrogen gas in air at room temperature (RT). By utilizing light, the working temperature of such gas sensors can be reduced whilst simultaneously enhancing sensing performance. In this study, sensors have been fabricated that introduces nano-Schottky junctions (Pd–$TiO_2$) via a facile chemical method and p–n heterojunctions (PdO–$TiO_2$), through both chemical and hydrothermal methods, with a mean Pd nanoparticle (NP) diameter of 4.98 ± 0.49 nm and 4.29 ± 0.45 nm, respectively. The hydrothermally treated Pd-decorated $TiO_2$ nanosphere (HPT NS) shows a response of 100.88% toward 500 ppm hydrogen with a faster response and recovery (77 s and 470 s, respectively). Meanwhile, hydrothermally untreated Pd-decorated $TiO_2$ (PT) NSs show a response of 100.29% with slow response and recovery times (240 s and 3146 s, respectively) at 30 °C under 565 nm visible light and a bias of 500 mV. The experimental results confirm that introducing both metallic Pd and PdO onto the $TiO_2$ NSs open a novel approach for detecting hydrogen gas through light-induced sensing at room temperature using low voltage bias.

**Keywords:** nanospheres; palladium; titanium dioxide; hydrogen sensing; visible light; hydrothermal method



**Citation:** Thathsara, T.; Harrison, C.J.; Hocking, R.K.; Shafiei, M. Pd- and PdO-Decorated $TiO_2$ Nanospheres: Hydrogen Sensing Properties under Visible Light Conditions at Room Temperature. *Chemosensors* **2023**, *11*, 409. https://doi.org/10.3390/chemosensors11070409

Academic Editors: Maria Josè Lo Faro and Salvo Mirabella

Received: 22 June 2023
Revised: 14 July 2023
Accepted: 18 July 2023
Published: 21 July 2023



## 1. Introduction

Hydrogen gas sensors play an important role in energy and industrial applications where the high flammability (ignition energy: 0.019 mJ) and explosiveness (presence of 4 to 75%) of hydrogen gas presents a substantial hazard [1]. With an increased investment in new hydrogen-based technologies, hydrogen gas is increasingly being used as a fuel for vehicles and power generation [2]. Hydrogen is considered a clean energy source and it produces no carbon emissions when burned or used in fuel cells to generate electricity. When hydrogen is burned, it combines with oxygen to produce water vapor, a harmless byproduct [3]. This makes hydrogen a promising alternative to traditional fossil fuels that emit harmful greenhouse gases when burned [4]. Furthermore, hydrogen sensors are used for the noninvasive diagnosis of medical conditions, including several gastrointestinal diseases [5]. Therefore, accurate and reliable hydrogen gas sensors are essential for maintaining safety, quality control and process monitoring in industrial settings, and present a promising avenue for medical research.

Advances in nanotechnology have enabled the development of highly sensitive and selective hydrogen sensing materials [6]. However, most of the developed sensing materials work only at high temperatures [7]. High-temperature hydrogen sensors can be prone to drift due to the degradation of the sensing layer over time. This poses safety issues and requires the assembly of heaters, leading to an increased manufacturing cost and high power consumption. Therefore, fabricating a hydrogen sensor that works at RT with low power consumption is important. However, it is still a challenging task. Light-induced

hydrogen gas sensing materials are poised to play a massive role in overcoming these limitations [8,9]. Sensing material under light conditions generates electron–hole pairs that can interact with oxygen and hydrogen gas molecules, causing them to either bind or dissociate from the material's surface easily [10]. These interactions alter the material's electrical properties, resulting in a measurable change in electrical conductivity that can be used to detect the presence of hydrogen gas at RT [11].

Considering the photoactive materials for hydrogen sensing applications, semiconductive metal oxide (SMO) materials have shown unique advantages due to their tunable surface properties. Recently, ZnO [12,13], $TiO_2$ [14,15] and $SnO_2$ [16] have all played a significant role in developing hydrogen sensors working at RT via photo-excitations. Among these SMO materials, $TiO_2$ has gained much attention due to its high chemical stability and sensitivity to hydrogen gas [17,18]. Additionally, $TiO_2$ is a low cost, abundant and environmentally friendly material, making it an attractive choice for hydrogen sensing applications. The wide band gap energy of $TiO_2$ (rutile, 3.30 eV and anatase, 3.57 eV) [19] makes it a promising photoactive material in hydrogen sensors that rely on light-induced changes in conductivity. However, $TiO_2$-based sensors have some limitations, including their relatively low sensitivity compared to other materials and the requirement for UV light (200–400 nm) to generate electron–hole pairs [20].

To synthesize a material highly sensitive toward hydrogen gas, researchers have used noble metals such as Pt, Au and Pd to introduce nano-Schottky junctions onto the sensing surface [21]. Additionally, the introduction of reduced graphene oxide (rGO) [22] and $MoS_2$ [23] to the sensing layer leads to the formation of heterojunctions (p–n) to create a more active depletion layer. Meanwhile, they have also implemented morphological changes (e.g., nanospheres, nano-flowers, nano-rods, etc.) in SMO materials to fabricate highly hydrogen-sensitive materials. In this research, we have fabricated $TiO_2$ NSs via the sol–gel method. The large surface area of the NSs allowed the deposition of Pd nanoparticles on the surface, thus forming nano-Schottky junctions between the $TiO_2$ and Pd. Furthermore, the fabricated Pd-decorated $TiO_2$ NSs were treated hydrothermally to introduce PdO and create p–n heterojunctions in the sensing layer. The formation of the nano-Schottky junctions and heterojunction on the $TiO_2$ NSs surface was confirmed by transmission electron microscopic (TEM) techniques, X-ray diffraction spectroscopic (XRD) technique, and Raman and X-ray photoelectron spectroscopy (XPS). Introducing PdO enhances the utilization of visible light by suppressing electron–hole recombination within the $TiO_2$ NSs.

## 2. Materials and Methods

### *2.1. Materials*

The chemicals to synthesize PT and HPT NSs, including 99.9% acetonitrile, 99.9% absolute ethanol, 28% ammonia solution, 97% titanium (IV) isopropoxide (TTIP), 97% (3-aminopropyl)triethoxysilane (APTS), sodium tetrachloropalladate (II) ($Na_2PdCl_4$), and sodium borohydride ($NaBH_4$)) were purchased from Sigma-Aldrich.

### *2.2. Synthesis of $TiO_2$ NSs*

$TiO_2$ NSs were fabricated based on previously published works [24,25]. Briefly, 0.91 mL of deionized (DI) water, 100 mL of 99.9% acetonitrile, 0.42 mL of 28% ammonia solution, and 150 mL of 99.9% absolute ethanol were mixed to prepare a uniform solution. Subsequently, 5 mL of 97% titanium (IV) isopropoxide (TTIP) was added to the solution, and the mixture was stirred for 6 h at room temperature (22 °C). The resulting precipitate was collected through centrifugation and subsequently washed multiple times with DI water. Finally, the precipitate was dried completely at 80 °C for 6 h. In the subsequent stage, the dried precipitate was subjected to calcination at 550 °C for a duration of 2 h.

### *2.3. Synthesis of Pd-Decorated $TiO_2$ NSs (PT NSs) and Hydrothermally Treated Pd-Decorated $TiO_2$ NSs (HPT NSs)*

For the preparation of APTS-modified $TiO_2$ NSs, an amount of 1.0 g of the pre-prepared $TiO_2$ NS was mixed with 20 mL of DI water. Subsequently, 6.20 mL of 97% of APTS was added gradually to the $TiO_2$ suspension, and the resulting mixture was subjected to stirring for a duration of 12 h at a temperature of 22 °C. Following the stirring process, the mixture was washed and rinsed three times with DI water. Finally, the resulting product was dried completely at 80 °C for 6 h until it reached a state of complete dryness.

An amount of 1.0 g of prepared $TiO_2$ NS was mixed with 20 mL of DI water to fabricate APTS-modified $TiO_2$ NSs. A total volume of 6.20 mL of 97% APTS was then gradually added to the $TiO_2$ suspension, and the mixture was then stirred for 12 h at 22 °C. The resulting mixture was washed and rinsed with DI water three times, and finally dried at 80 °C for 6 h until completely dry. For Pd decorations, subsequently, a mixture of 8.6 mg of $Na_2PdCl_4$ and 50 mg of calcined APTS-modified $TiO_2$ NS was added to 30 mL of DI water and stirred for 2 h at 22 °C. Then, the solution containing 20 mL of 0.0660 moldm$^{-3}$ $NaBH_4$ was added to the mixture and stirred for an additional 1.5 h to fully decorate the $TiO_2$ NSs with Pd nanoparticles. The resulting precipitate was collected and dried at 80 °C for 6 h to ensure complete dryness and for further use. An amount of 50 mg of Pd-decorated $TiO_2$ NS was dispersed in DI water and then the mixture was transferred into the Teflon-lined autoclave, and it was placed in an oven at 180 °C for 12 h to form Pd- and PdO-decorated $TiO_2$ NSs (HPT NSs) as shown in Scheme 1.

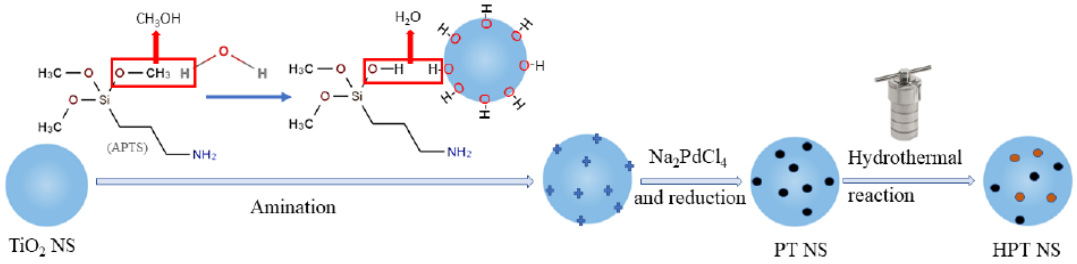


**Scheme 1.** Synthesis procedure of PT and HPT NSs.

### *2.4. Sensor Fabrication*

An amount of 10 mg of synthesized PT and HPT NS was dispersed in 10 mL of DI water separately and sonicated for 2 min. Afterward, 10 µL of dispersion was deposited on 10 × 6 mm gold interdigitated electrodes with a finger spacing of ~10 µm (IDE, purchased form Micrux Technologies). Finally, it was dried at 80 °C for 15 min.

### *2.5. Material Characterization*

Using a scanning electron microscope (SEM, Hitachi S-4800) equipped with a field emission gun, a morphological analysis of the synthesized PT and HPT NSs was investigated. Additionally, transmission electron microscopy (TEM, Tokyo, Japan) was performed using a JEOL 2100 TEM instrument to determine d spacings. Elemental distribution was determined through energy-dispersive X-ray spectroscopy (EDS) analysis using an Oxford XMax system (High Wycombe, UK). To investigate the phase compositions of the materials, a Bruker X-ray diffractometer (XRD, Bremen, Germany) D8 advanced with a mixture of CuKα1 and CuKα2 sealed tube (1.5406 nm) and a Lynxeye detector were employed. Raman spectra were obtained for PT and HPT NSs using a Renishaw inVia Raman spectroscope (Gloucestershire, UK) equipped with a 514.5 nm laser. For the analysis of photoactivity, UV–visible diffuse reflection spectra were collected using a PerkinElmer Lambda 1050 UV/VIS/NIR spectrometer (Massachusetts, USA). The elemental compositions of the synthesized materials were analyzed using X-ray photoelectron spectroscopy (XPS) spectra with a Kratos Analytical, Inc. instrument based in Manchester, UK.

### 2.6. Sensor Measurements

In the experimental investigation, synthesized PT and HPT NSs were subjected to hydrogen gas testing within a custom-built, fully automated and enclosed chamber. The chamber consists of a temperature- and humidity-controlled Linkam stage (T96, LINKAM Scientific Instruments Ltd.) (Tadworth, UK) to maintain precise environmental conditions. The gas flow was regulated using seven mass flow controllers (MKS GE50A and AliCat MC-Series, MFCs) (Andover, MA, USA), ensuring accurate control over the flow rates. To introduce controlled humidity levels, a humidity generator (LINKAM RH95) was incorporated into the experimental setup. Additionally, a built-in heater was employed to maintain the desired temperature during the testing process.

In order to investigate the response of the sensor, hydrogen gas with varying concentrations (50 to 1000 ppm) were generated by diluting the gas with dry, instrument-grade synthetic air (21% $O_2$ in $N_2$ balance). This was achieved using mass flow controllers (MFCs) at a constant flow rate of 200 standard cubic centimeters per minute (sccm). Dry synthetic air as a reference gas was used for dilution and maintaining consistent conditions. Each experiment involved a gas exposure time of 3 min, followed by a purging phase of 1 h using synthetic air to ensure thorough removal of any residual gases and maintain the baseline.

To monitor and measure the response of the sensor during the experiments, a Keithley Piccoammeter (model 6487) from Cleveland, OH, USA, was employed. This instrument periodically recorded interval currents at specific time points. The sensor's response to the target gas was evaluated by measuring the change in current while exposed to the calibrated hydrogen gas. The current measurements were obtained at a bias voltage of 500 mV. Subsequently, the obtained current values were correlated to the corresponding gas concentrations, allowing for the assessment of the sensor's sensitivity to hydrogen gas.

The developed materials were tested at a bias of 500 mV and operating temperatures ranging from 25 to 80 °C under 565 nm visible light. To illuminate the sensor surface, a Thor Labs M565D$^{2g}$ light source was utilized. The light source was driven at a constant current of 1000 mA. It was positioned on top of the stage with a distance of 2 cm from the sensor surface. This setup resulted in an irradiance of approximately 1170 $\mu W/mm^2$, providing the necessary optical energy for the experimental measurements. The sensor performance was evaluated in terms of response magnitude, selectivity, response time, recovery time, stability and limit of detection (LOD) toward varying concentrations of hydrogen gas up to 1% under different operating conditions such as temperature and light. Selectivity was tested toward 50 ppm of ammonia ($NH_3$), methane ($CH_4$) and nitrogen dioxide ($NO_2$) and 500 ppm of carbon dioxide ($CO_2$) at optimal operating conditions. All the gases were calibrated and purchased from Coregas, Australia. Additionally, the effect of humidity on the sensing performance was also investigated. These test conditions were balanced with synthetic dry air, keeping a constant flow rate of 200 $cm^3$/min. Finally, sensor response magnitude and response ($R$%) were calculated using Equations (1) and (2), respectively. The response time ($t_{res}$) and recovery time ($t_{rec}$) were evaluated as the time required for the sensor to reach 90% of its maximum response and to recover to 10% of its baseline, respectively [26].

$$Response\ magnitude = I_{gas} - I_{air} \quad (1)$$

$$Response\ (R\%) = \left(\frac{I_{gas}}{I_{air}}\right)\% \quad (2)$$

$I_{air}$: Current of the sensor in the baseline condition (i.e., in air).
$I_{gas}$: Current of the sensor in hydrogen environment.

## 3. Results and Discussions

### *3.1. Material Characterization*

In this study, spherical-shaped $TiO_2$ NSs were fabricated via a sol–gel technique to enhance the particle surface-to-volume ratio. As shown in Figure 1a, the rigid agglomeration of free $TiO_2$ nanospheres (NSs) can be seen, with a calculated mean diameter of 429 ± 0.05 nm. Pd nanoparticles (NPs) were then decorated on the surface of the synthesized $TiO_2$ NSs to enhance the hydrogen sensing performances. According to the TEM imaging of PT NSs (Figure 1b), granular shaped, agglomeration-free, and unevenly dispersed Pd NPs can be seen on the surface of $TiO_2$ NSs with a calculated mean diameter of 4.98 ± 0.49 nm. Furthermore, as shown in Figure 1c, lattice spacings of 0.22 nm originated from the surface of the $TiO_2$ NSs and corresponded to the (111) lattice plane of face-centered cubic Pd NPs [27]. Therefore, the formation of nano-Schottky junctions between $TiO_2$ NSs and the Pd NPs is also revealed. It was calculated that the *d* spacing of 0.24 nm can be attributed to the presence of anatase-phase $TiO_2$ NSs [28]. To compare these results with HPT NSs, SEM (Figure 1d) and TEM (Figure 1e) images were obtained. As shown in Figure 1d, rigid, agglomeration-free nano-sized spheres (mean diameter 680 ± 0.05 nm) can be seen. It was revealed that the hydrothermal treatment process increased the diameter from 429 nm (pre-treatment) to 680 nm (post-treatment) while maintaining the nanosphere shape. However, the mean diameter of Pd NPs was reduced from 4.98 nm (pre-treatment) to 4.29 ± 0.45 nm (post-treatment) with the *d* spacings of 0.12 nm and 0.13 nm (Figure 1f), which correspond to the (220) and (311) planes of face-centered cubic Pd, respectively [29]. Therefore, significant changes are observed when considering the lattice planes of Pd after hydrothermal treatment.

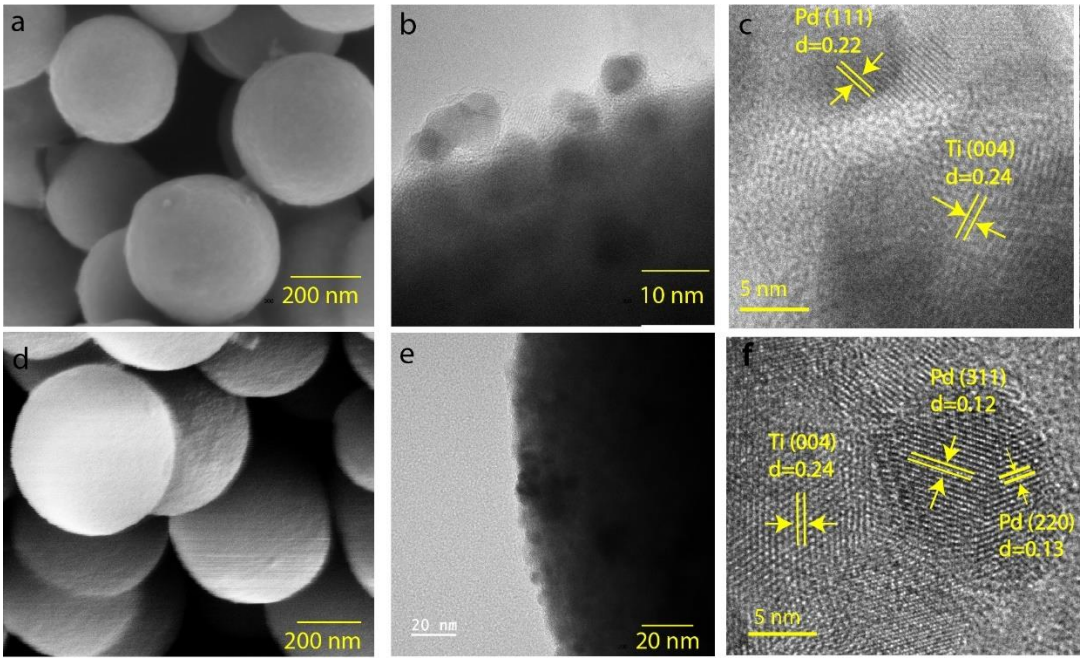


**Figure 1.** (**a**,**d**) SEM, (**b**,**e**) TEM and (**c**,**f**) HR-TEM images for PT and HPT NSs, respectively.

Considering the EDS elemental mapping results (Figure 2) of PT and HPT NSs, randomly dispersed Pd NP-enriched $TiO_2$ NSs can be observed. Furthermore, these results confirmed the presence of Ti, O, C and Si. The presence of C and Si on synthesized materials demonstrated that the modification of $TiO_2$ NSs with APTS was conducted properly. These results confirmed the decoration of Pd NPs with random distribution on the surface of $TiO_2$ NSs in PT (Figure 2b) as well as HPT NSs (Figure 2f).

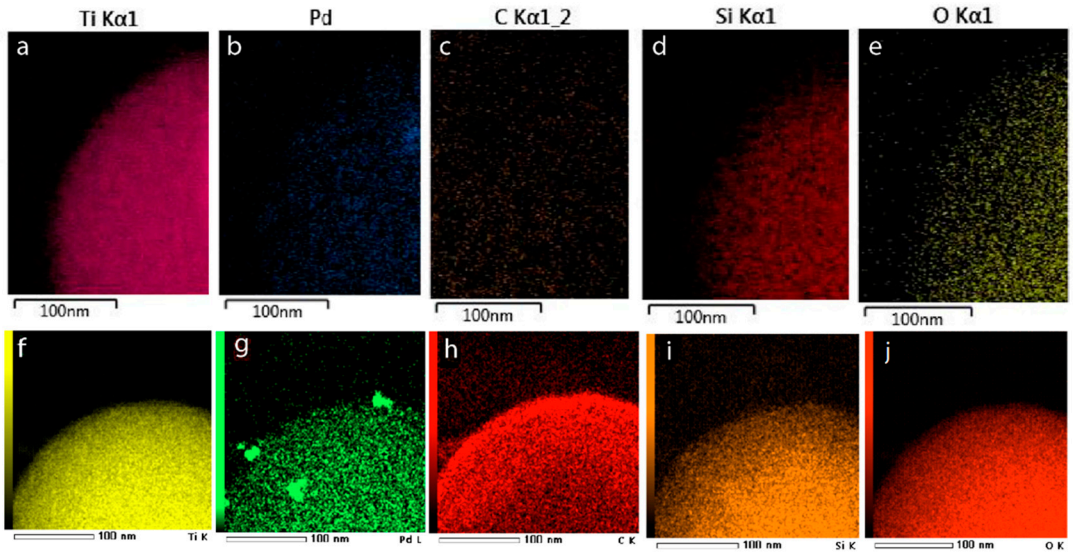


**Figure 2.** EDS images of (**a**) Ti, (**b**) Pd, (**c**) C, (**d**) Si and (**e**) O for PT NSs and (**f**) Ti, (**g**) Pd, (**h**) C, (**i**) Si and (**j**) O for HPT NSs.

To investigate the phase composition of the synthesized PT and HPT NSs, XRD (Figure 3a) and Raman (Figure 3b) analyses were conducted. Moreover, UV–Vis diffuse reflectance spectra (DRS) were obtained for both PT and HPT NSs to investigate their photoactivity under 200–700 nm wavelength light (Figure 3d) to calculate band gap energy. According to the XRD results, prior to modification with APTS, the highly crystalline nature of the $TiO_2$ NSs resulted in the observation of strong diffraction peaks. Specifically, the observed peaks at 25.20°, 37.76°, 47.96°, 56.64° and 62.78° can be attributed to the crystal planes (101), (004), (200), (105) and (204), respectively, belonging to the anatase phase of $TiO_2$ NSs (JCPDS No. 21-1272) [30]. Furthermore, the peaks at 27.48°, 41.20°, 54.33° and 69.04° corresponded to the crystal planes (110), (111), (220) and (112), respectively, indicating the presence of the rutile phase in the synthesized $TiO_2$ NSs, as indicated by JCPDS No. 76-1939 [31]. After the modification of $TiO_2$ NSs with APTS, the clear peaks attributed to the anatase and rutile phases of $TiO_2$ were not visible due to interference with APTS [24]. Therefore, Raman spectra were obtained for further analysis of the presence of phases in the synthesized $TiO_2$ modified with APTS, PT NSs and HPT NSs. According to the Raman active modes in the vibrational spectra that correspond to the $TiO_2$ NSs were observed at around 144 ($E_{g(1)}$), 194 ($E_{g(1)}$), 396 ($B_{1g}$), 516 ($A_{1g}$) and 638 ($E_{g(1)}$) $cm^{-1}$, corresponding to the anatase phase [32], and meanwhile, 445 ($E_{g(1)}$) and 612 ($A_{1g}$) $cm^{-1}$ peaks were observed for the rutile phase [33] of the prepared $TiO_2$ NSs. However, after modification with APTS and Pd, noticeable peak shifts can be observed in the Raman spectra. These shifts are attributed to changes in molecular bonding. Furthermore, when analyzing the Raman spectra of HPT NSs, distinct peaks at 146 ($E_{g(1)}$), 402 ($B_{1g}$), 516 ($A_{1g}$) and 633 ($E_{g(1)}$) $cm^{-1}$ were observed, indicating the presence of the anatase phase of $TiO_2$ NSs. Additionally, a peak at 246 ($E_{g(2)}$) $cm^{-1}$ can be observed and which corresponds to the rutile phase of $TiO_2$ NSs [34]. Optical properties of the fabricated $TiO_2$ NSs, PT NSs and HPT NSs were investigated using UV–Vis diffuse spectrometer. According to Figure 3c, in the spectra that correspond to the $TiO_2$ NSs, PT NSs and HPT NSs, a sharp rise in the intensity of absorbance was detected for wavelengths below 423 nm, indicating the presence of a bandgap transition specifically at this wavelength. The corresponding bandgap values were determined using the Kubelka–Munk indirect function (Figure 3d) [35] and values were calculated to be approximately 2.91, 2.87 and 2.16 eV for the $TiO_2$ NSs, PT NSs and HPT NSs, respectively. Based on the results obtained from the UV–Vis diffuse spectrometer, the synthesized HPT NSs demonstrated activity in both the UV range (200–400 nm) and the visible light range (400–700 nm).

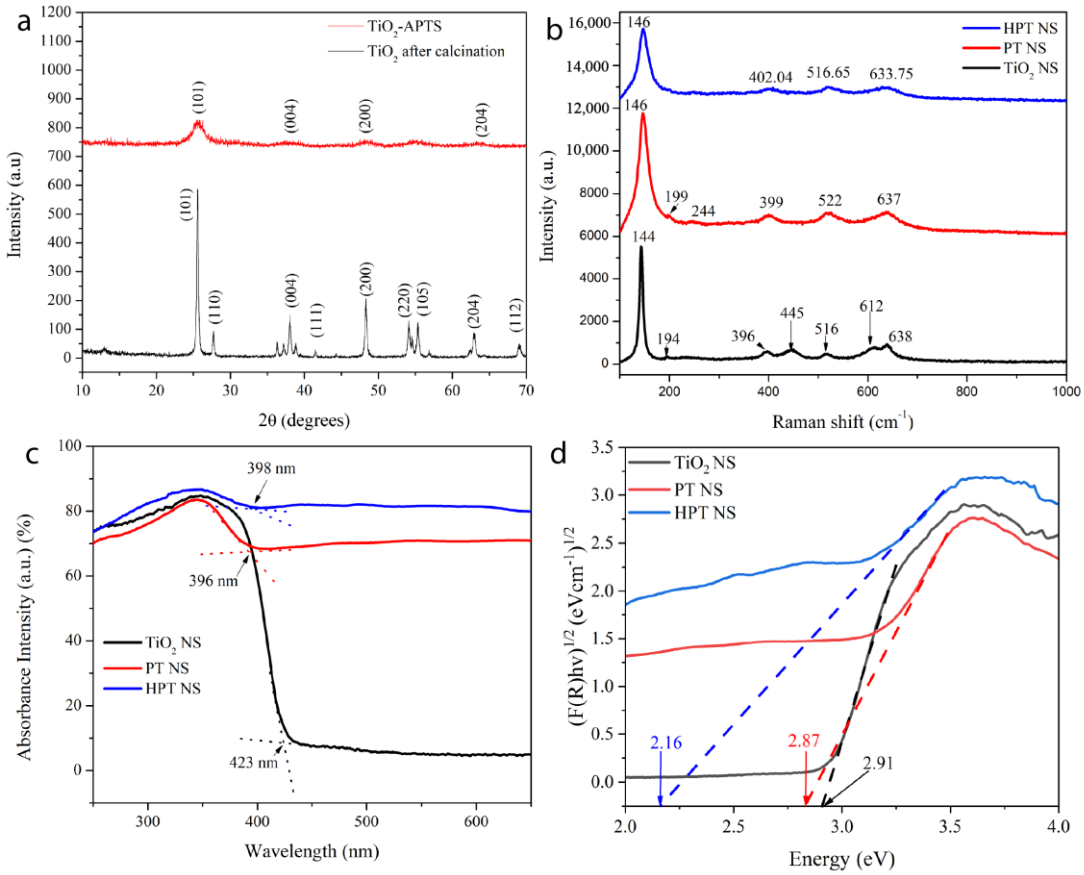


**Figure 3.** (**a**) XRD spectra of $TiO_2$ NSs. (**b**) Raman spectra, (**c**) UV-Vis diffuse reflectance and (**d**) Kubellka-Munk indirect function spectra for $TiO_2$ NSs, PT NSs and HPT NSs.

To examine the chemical composition and electronic states of the elements of synthesized PT and HPT NSs, XPS analysis was performed. According to Figure 4a, wide spectra of $TiO_2$ NSs, PT and HPT NSs confirmed the absence of surface contaminants and the presence of the Ti 3p, Ti 2s, C 1s, Pd 3d, Ti 2p, Ti 2s, O 1s and O kα1. As shown in Figure 4b, two significant peaks can be found for PT NSs at 455.88 and 461.63 eV, while for HPT NSs, the peaks were observed at 455.63 and 461.41 eV corresponding to the Ti $2p_{3/2}$ and Ti $2p_{1/2}$, due to the presence of $Ti^{4+}$ oxidation states [36]. Comparing the obtained results of Ti 2p, we can observe a negative peak shift of around 0.2 eV after treating hydrothermally. Moreover, considering the XPS spectra of O 1s for PT and HPT NSs (Figure 4c), the same kind of negative peak shifts are observed. The result indicates that hydrothermal treatment could enhance the number of oxygen vacancies in $TiO_2$ [37]. Furthermore, considering the O 1s spectrum of HPT NSs (Figure 4d), two significant peaks were observed around 526.97 and 529.33 eV, which can be attributed to the formation of lattice oxygen (Ti–O) and physically adsorbed water (Ti–OH) during the sol–gel synthesis and hydrothermal process [38]. Comparing the peak intensities around 529 eV, significantly high intensities were observed for HPT NSs, and it was clearly indicated that the hydrothermal process introduces more Ti–OH as well. Finally, The Pd 3d spectrum was analyzed to identify the oxidation states of Pd. It revealed the presence of two distinct states. Notably, the Pd $3d_{5/2}$ deconvolution showed an intense peak at 331.81 and 337.15 eV for PT NSs, which correspond to the metallic Pd state, while peaks around 331.01 and 338.13 eV could indicate a partial oxidation of Pd, leading to the formation of a PdO structure [39]. Therefore, the carefully analysis of Pd 3d spectrum of HPT NSs confirms the presence of Pd and PdO. Furthermore, with the careful analysis of a deconvoluted Pd 3d spectrum of HPT NSs, the absence of Pd–PdO interfacial layers is confirmed [40].

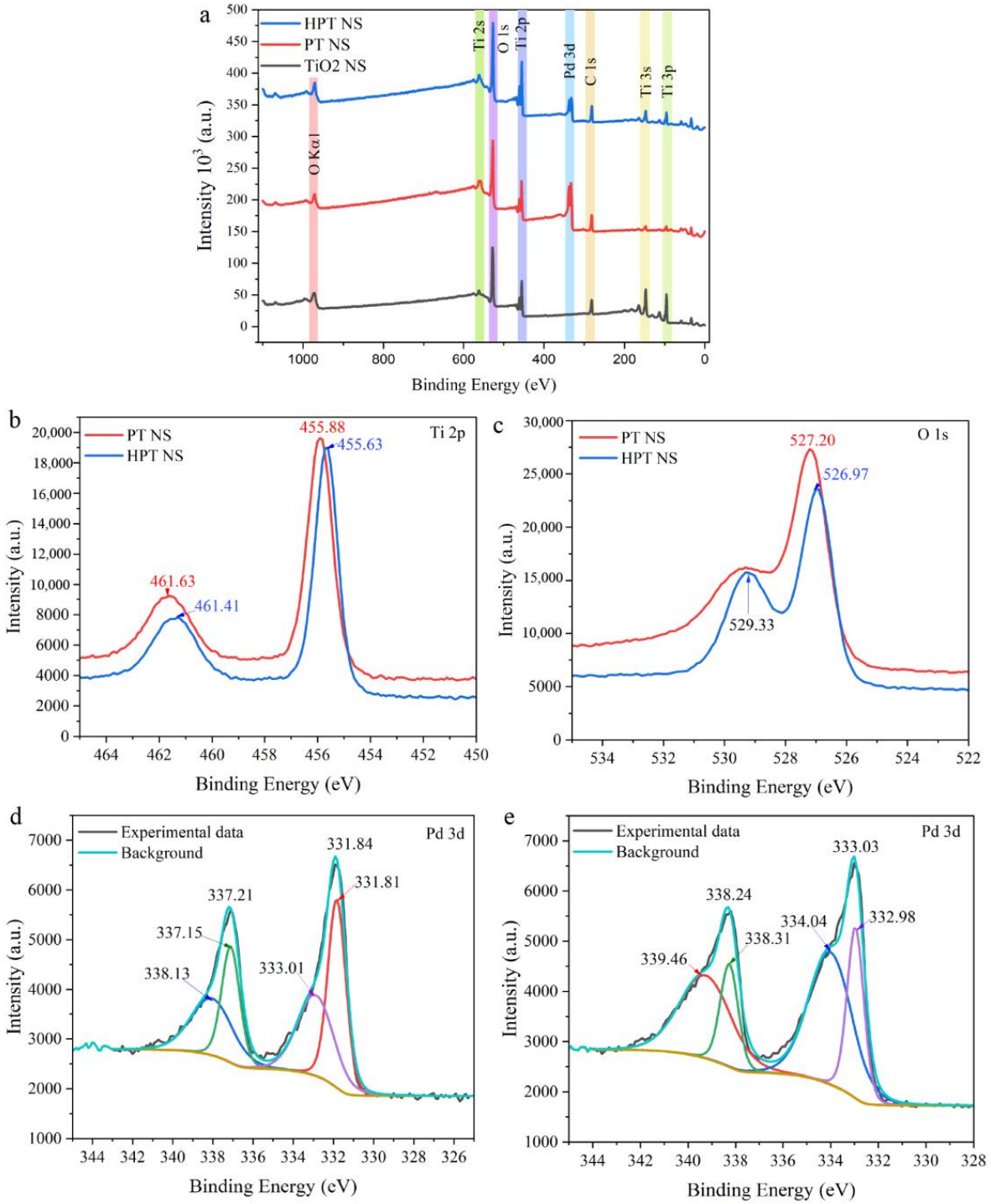


**Figure 4.** XPS spectra for (**a**) the wide spectra of $TiO_2$, PT and HPT NSs, the comparison of (**b**) Ti 2p, (**c**) O 1s, (**d**) deconvoluted O 1s for HPT NSs and (**e**) Pd 3d spectra for PT and HPT NSs.

### *3.2. Hydrogen Sensing Characterization*

The aim of this study was to fabricate highly hydrogen-sensitive and selective materials that work at low temperatures, voltages and visible light conditions. Thus, light-assisted chemiresistive hydrogen sensors were tested to find optimal operation conditions. The sensing performance of HPT NSs at different voltage biases (10, 50, 100 and 500 mV) was studied at 30 °C under dark conditions. The respective calculated response (%) and response and recovery times are tabulated in Table 1.

**Table 1.** Sensor response (%) and response and recovery times of HPT NSs for 500 ppm hydrogen at 30 °C under dark conditions at different voltages biases.

| Voltage (mV) | Response (%) | Response Time (s) | Recover Time (s) |
|---|---|---|---|
| 10 | 100.85 | 270 | 3300 |
| 50 | 100.97 | 183 | 3036 |
| 100 | 100.97 | 240 | 2640 |
| 500 | 101.12 | 180 | 1680 |

The applied potential, (i.e., voltage), shows a significant influence on the response and recovery times, whilst leaving the response itself unaffected. Higher applied potentials generally lead to faster response and recovery times due to the increased driving force generated by a higher potential, allowing electrons and anions present in the synthesized HPT NSs to move and react more quickly. As a result, the system exhibits a quicker response and recovery time [10].

Importantly, it should be noted that the applied potential does not directly modify the response itself. The response is primarily determined by the intrinsic properties and active sites present in the synthesized PT and HPT NSs.

The voltage bias of 500 mV was used to evaluate hydrogen sensing properties at different temperature conditions in dark conditions. The optimum temperature of 50 °C was identified and the calculated sensor response, and response and recovery times are presented in Table 2. As seen in Figure 5a, sensor response magnitude increased as the operating temperature was raised from 25 °C to 50 °C due to the accelerated adsorption/desorption kinetics between the hydrogen and HPT NSs [41]. Furthermore, an increase in the operating temperature to 80 °C resulted in a decrease in the sensing response, attributed to the Langmuir effect [42]. The PT NSs-based sensors did not stabilize under dark conditions.

**Table 2.** Sensor response (%) and response and recovery times of HPT NSs at different temperatures under dark conditions and 500 mV voltage bias.

| Temperature (°C) | Response (%) | Response Time (s) | Recover Time (s) |
|---|---|---|---|
| 25 | 101.04 | 144 | 11,990 |
| 30 | 101.14 | 100 | 1680 |
| 35 | 101.14 | 114 | 1345 |
| 40 | 101.16 | 110 | 1380 |
| 45 | 101.23 | 110 | 1380 |
| 50 | 101.26 | 135 | 1345 |
| 60 | 101.19 | 55 | 2310 (unstable baseline) |

Moreover, according to Table 2, a change in response time and recovery time by increasing the temperature can be attributed to the impact of temperature on hydrogen molecule desorption and adsorption rates. When the temperature reaches the optimum temperature (i.e., 50 °C), a higher desorption rate is obtained compared to the adsorption rate (Langmuir effect) [42,43]; therefore, the sensor exhibits faster response and recovery times. According to the obtained results, it is evident that optimizing the operating temperature is a crucial factor in attaining the desired sensing performance.

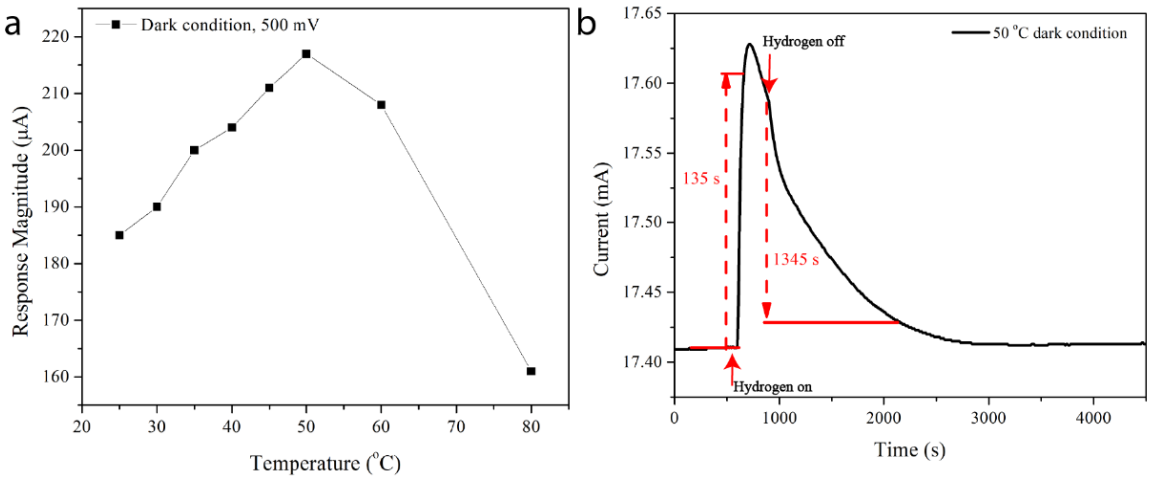


**Figure 5.** HPT NSs: (**a**) Response magnitude as a function of temperature and (**b**) response and recovery times for 500 ppm hydrogen at 50 °C under dark conditions and 500 mV.

Based upon the calculated response and recovery times of the HPT NSs for 500 ppm hydrogen gas (Figure 5b), it was observed that these times were considerably prolonged in the absence of light. To improve upon the slow response and recovery times, various wavelengths under both UV range (200–400 nm) and visible range (400–700 nm) were employed. Under light conditions, the optimum wavelength was investigated at 30 °C and 500 mV bias. According to Table 3, the optimum hydrogen sensing properties were obtained under 565 nm wavelength. Furthermore, the calculated sensor response (%), and response and recovery times for different wavelengths were tabulated in Table 3. As shown in Figure 6a, the response and recovery times were drastically improved (reduced from 100 s to 77 s for response time and from 1680 s to 470 s for recovery time) under the 565 nm light conditions compared to the dark conditions at 30 °C while maintaining the sensor response (%). At 50 °C under 565 nm, the response and recovery were improved from 135 to 110 s and from 1345 to 1303 s, respectively (Figure 6b). The results suggest that hydrogen sensing in the presence of light conditions results in the generation of a greater number of electron–hole pairs, facilitating the formation of photo-induced physiosorbed oxygen ions [8]. As a result, response and recovery times improved significantly while maintaining the sensor response for 500 ppm hydrogen.

**Table 3.** Sensor response (%) and response and recovery times of HPT NSs under dark and different wavelengths at 30 °C and 500 mV voltage bias.

| Wavelengths (nm) | Response (%) | Response Time (s) | Recover Time (s) |
|---|---|---|---|
| Dark condition | 101.08 | 100 | 1680 |
| 365 | 101.00 | 210 | 1470 |
| 490 (blue light) | 101.08 | 168 | 694 |
| 530 (green light) | 101.12 | 106 | 640 |
| 565 (yellow light) | 100.82 | 77 | 470 |
| 625 (orange light) | 100.82 | 154 | 660 (not fully recovered) |

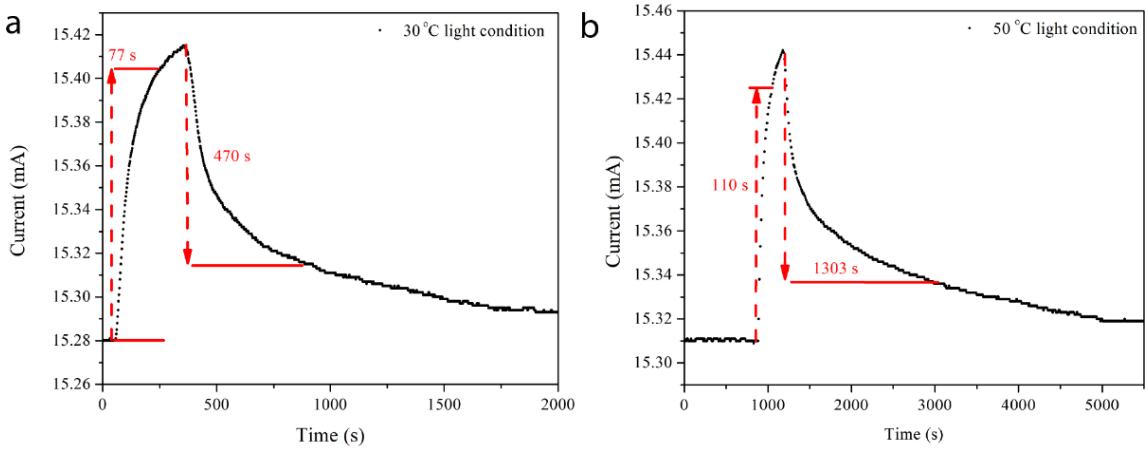


**Figure 6.** HPT NSs: Response and recovery times for 500 ppm hydrogen at (**a**) 30 °C and (**b**) 50 °C under 565 nm light condition and 500 mV.

Figure 7 shows the sensor response toward hydrogen with different concentrations (50–1000 ppm) at 30 °C under 565 nm light and dark conditions with 500 mV bias. Under dark conditions, a higher response (%) was observed compared to light conditions for hydrogen, with responses of 100.54% and 101.18% to 500 ppm hydrogen, respectively. However, incomplete recovery with non-linearity ($R^2$ = 0.75) was also observed. Because the sensing mechanism mainly relies on the adsorption process of environmental oxygen, here, mainly physisorption and chemisorption processes involve adsorbing oxygen and hydrogen. However, chemisorbed oxygen species are chemically stable and require more energy to desorb from the sensing material [44]. Therefore, the recovery time was prolonged under dark conditions, and the sensing material became saturated at very low hydrogen concentrations, at 250 ppm of hydrogen (Figure 7a). According to the sensor response under 565 nm visible light condition (Figure 7a,b), an improved recovery is observed and the saturated point can be extended up to 750 ppm hydrogen with linear regression ($R^2$ = 0.99). Moreover, the sensitivity of HPT NSs toward hydrogen was calculated to be 1.02 µA/ppm at 30 °C under 565 nm visible light condition. To identify the limits of detection (LOD) of HPT NSs, according to the IUPAC instructions [45], the three standard deviations of the sensor's response in dry air (baseline) was obtained, and using Equation (3), a lower detected concentration was calculated as 2.03 ppm at 30 °C under 565 nm visible light condition with 500 mV bias.

$$C_L = \frac{KS_B}{m} \quad (3)$$

where, $m$ corresponds to the slope (sensitivity) of the calibration curve; $k$ is a numerical factor chosen in accordance with the confidence level desired, and the use of $k$ equals to 3 allows for a confidence level of 99.86% of the normal distribution curve; $S_B(\sigma)$ is the standard deviation of the sensor baseline corresponding to the dry air (baseline); and $C_L$ is the calculated LOD value.

In chemiresistive hydrogen sensors, the signal-to-noise ratio (SNR) can be calculated using the sensor signal as a response magnitude and the noise level. In this study, the SNR calculation was calculated with respect to a hydrogen concentration of 500 ppm. The noise level was determined using the baseline signal, which represents the average or expected response of the sensor in the absence of hydrogen gas. To calculate the noise level, the standard deviation of the base line was calculated and then the standard deviation was multiplied by three. The SNR was calculated at 30 °C under 565 nm visible light conditions with 500 mV bias to assess the quality of the signal produced by the HPT NSs relative to the level of background noise present. The calculated value was 62.62, and the obtained signals from HPT NSs in response to hydrogen indicated an improved signal quality and enhanced reliability for the detection and interpretation of the signal. For comparison, the PT NSs was tested toward hydrogen with concentrations ranging from 50 to 1000 ppm at 30 °C,

under visible light conditions (wavelength of 565 nm) and with a voltage bias of 500 mV (Figure 8a). Significant baseline noise was detected throughout the experimental period. Consequently, the SNR was calculated for PT NSs as 5.04. This value was significantly lower compared to the HPT NSs with a magnitude of 12.42. Furthermore, a response of 100.29%, response and recovery times of 240 s and 3136 s, respectively, were calculated for the PT NSs toward 500 ppm hydrogen (Figure 8b).

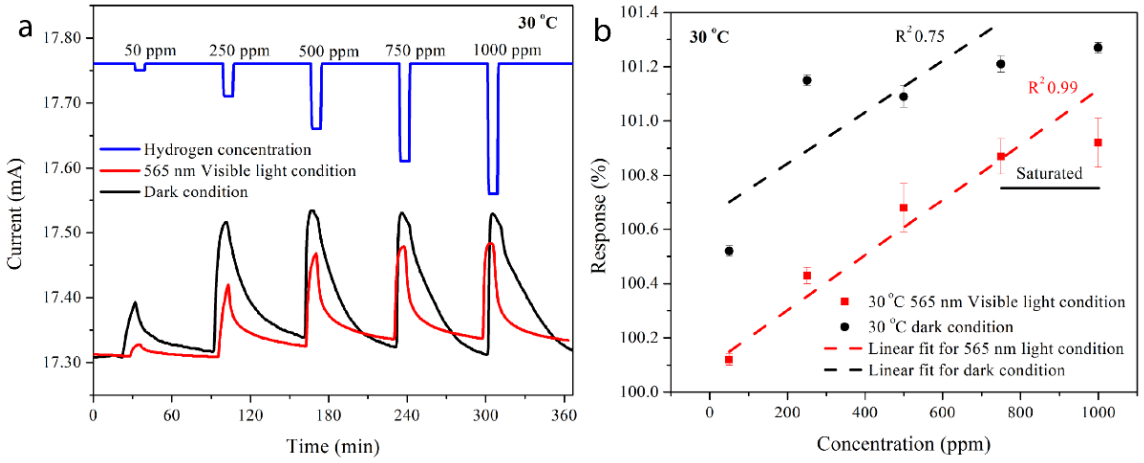


**Figure 7.** HPT NSs: (**a**) Sensor response toward hydrogen with different concentrations (250 to 1000 ppm) and (**b**) respective sensor response vs. concentration at 30 °C under 565 nmwith 500 mV bias.

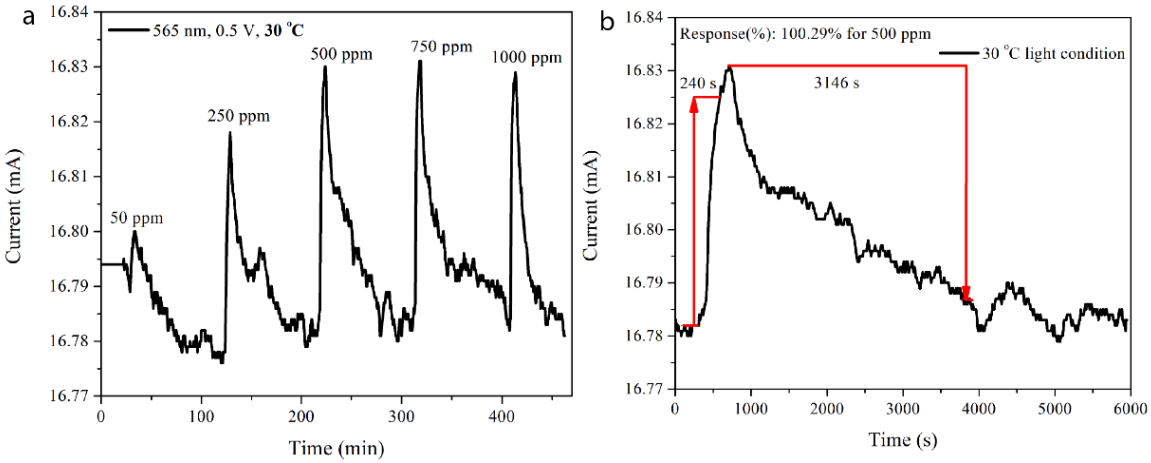


**Figure 8.** PT NSs: (**a**) Sensor response toward hydrogen (250 to 1000 ppm) and (**b**) response and recovery times for 500 ppm hydrogen at 30 °C under 565 nm visible light conditions with 500 mV.

To assess the selectivity of HPT NSs, various interfering gases commonly encountered in both natural environmental and industrial conditions were examined. The sensors were also tested toward 500 ppm $CO_2$, 50 ppm $CH_4$, 50 ppm $NH_3$ and 50 ppm $NO_2$ at 30 °C, under 500 mV bias with a wavelength of 565 nm. The obtained results are presented relative to the response toward 50 ppm hydrogen (Figure 9) with a response of 0.99%, 1%, 0 and 0.99% for 500 ppm $CO_2$, 50 ppm $CH_4$, 50 ppm $NH_3$, and 50 ppm $NO_2$, respectively. The sensor exhibits a p-type response toward $CO_2$ and $NO_2$ (oxidizing gases). The calculated relative response (%) toward the interference gases was significantly low. Therefore, synthesized HPT NSs can be effectively utilized for hydrogen sensing within its calculated detection range (i.e., 50–750 ppm) under real environmental conditions in the presence of other interfering gases. Furthermore, the sensor response (%) toward 50 ppm hydrogen was studied under 10% relative humidity (RH) conditions at 30 °C, under 500 mV bias with a wavelength of 565 nm, and it showed an enhancement in the response (100.20%), which

could be due to the presence of hydroxyl active sites on the sensing layer acting as electron donors. This enhances the electric charge density by facilitating the formation of hydronium cations from ionized water molecules as $2H_2O \leftrightarrow OH^- + OH_3^+$ [46,47]. Table 4 summarizes the comparison of hydrogen sensing performance (response, response and recovery times) between selected Pd- and PdO-based nanomaterials with the current study.

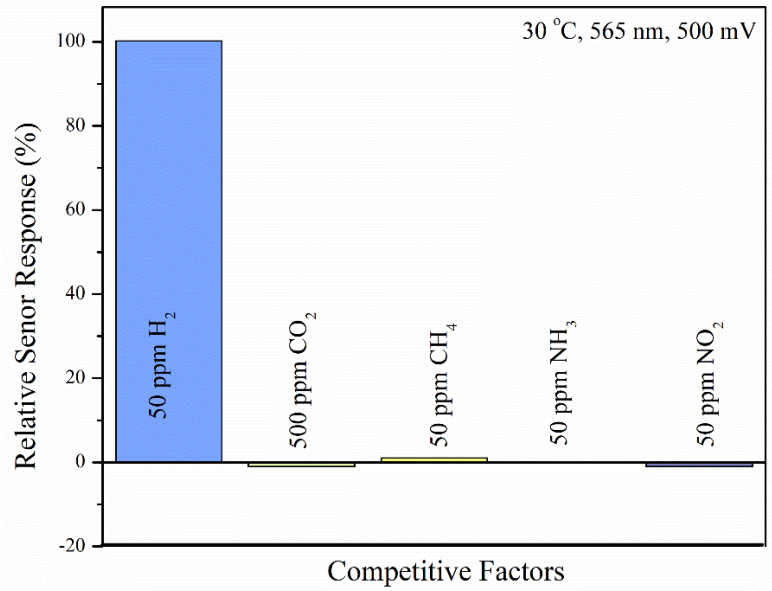


**Figure 9.** Selectivity for HPT NSs at 30 °C under 565 nm visible light conditions with 500 mV bias.

**Table 4.** Comparison of hydrogen gas sensing parameters of HPT NSs with recently published research work.

| Sensing Material | Applied Voltage (V) | Concentration (ppm) | Temperature (°C) | Light Source | Response | Response/Recovery Times (s) | Ref. |
|---|---|---|---|---|---|---|---|
| $TiO_2$–Pd Long-range-ordered crystals (LROC) | 9 | 500 | 33 | UV (365 nm) | 91% [a] | 45/24 | [40] |
| Pd–$MoS_2$ | 3 | 140 | 25 | Visible light | 17.45% [c] | 351/515 | [23] |
| PdO Thin films | - | 2% | RT ($N_2$ as carrier gas) | - | - | 10/10 | [48] |
| Pd–PdO Nanospheres | 1 | 1% | RT | - | 160% [a] | 5/32 | [49] |
| PdPt@ZnO Core shell nanoparticles | - | 100 | 350 | - | 48 [b] | 0.7/3 min | [50] |
| Pd/$TiO_2$ Two-dimensional Porous $TiO_2$ | - | 1000 | 230 | - | 9 [c] | 1.6/1.4 | [51] |
| PdO-loaded $WO_3$ Nanohybrids | - | 40 | RT | 450–490 nm Visible light | 8.02 [b] | 2.1/5.8 min | [52] |
| PdPdO@$TiO_2$ Nanospheres | 0.5 | 500 | 30 | 565 nm Visible light | 100.82% [d] | 77/470 | This research |

[a] $\frac{R_{gas}-R_{air}}{R_{air}} \times 100\%$, [b] $\frac{R_{gas}-R_{air}}{R_{air}}$, [c] $\frac{R_{air}}{R_{gas}}$, [d] $\frac{I_{air}}{I_{gas}} \times 100\%$. N/A: Not available. $R_{air}$ and $R_{gas}$: Resistance in air and target gas, respectively.

According to Table 4, we have successfully synthesized a visible-light active Pd- and PdO-introduced $TiO_2$ NS, that operates at a temperature of 30 °C under a low voltage bias of 500 mV. This material exhibits the capability to detect low concentrations of hydrogen gas with improved response and recovery times. The integration of both Pd and PdO nanoparticles with $TiO_2$ NSs as a proof-of-concept demonstrates a promising pathway for hydrogen gas sensing at 30 °C, employing light-induced mechanisms. This innovative

approach highlights the potential for advancements in the field of hydrogen gas sensing, thereby opening up new avenues for research and technological development.

### *3.3. Hydrogen Sensing Mechanism*

Referring to Figure 1c,f, the Pd NPs are directly contacted with $TiO_2$ NSs, forming nano-Schottky junctions, while the PdO presence in HPT NSs forms PdO–$TiO_2$ (p–n) heterojunctions. As a result, both nano-Schottky and p–n heterojunctions need to be considered in hydrogen gas sensing mechanism. However, based on the XPS results for PT NSs, only Pd–$TiO_2$ nano-Schottky junctions could be identified. The key identification in PT NSs was the absence of p–n heterojunctions. Therefore, these experimental findings revealed the significance of incorporating p–n heterojunctions to enhance hydrogen sensing at RT under visible light conditions. In semiconductive metal-oxide-based gas sensors, the gas sensing mechanism mainly relies upon resistance changes caused by the adsorption and desorption of the target gases and presence of the oxygen in air. Under natural air conditions, the chemisorbed and physiosorbed oxygen species play a significant role for sensing through the formation of depletion layers on the surface of the $TiO_2$ grain boundaries.

As shown in Figure 10a, undercoordinated pentacoordinate Ti cations ($Ti_{5c}$) and bidentate oxygen anions ($O_{2c}$), as well as fully coordinated Ti cations ($Ti_{6c}$) and tridentate O anions ($O_{3c}$), could attribute to the $TiO_2$ anatase (101) phase, and it has the same periodicity as the bulk-truncated surface [53]. Considering the $O_2$ adsorption process, two significant models can be found in the recently published research works [54]. As shown in Figure 10b, the two models can be explained as two atoms in the O molecule positioned on top of: (1) one $Ti_{5C}$ atom and (2) two $Ti_{5C}$ atoms on the (101) surface. In this study, the material works at 30 °C under 565 nm light condition; therefore, the dominant oxygen species might be $O^-_{2(hv)}$. Furthermore, based on the literature, the work function values for PdO, $TiO_2$ and Pd are 5.29 eV, 4.21 eV and 5.22 eV [55], respectively. Therefore, electron flow began from $TiO_2$ NSs to Pd and PdO. Under the 565 nm light condition, the chemisorbed $O^-_{2(ads)}$ reacts with the holes n the valance band of $TiO_2$ as well as PdO and form physiosorbed $O_{2(gas)}$. Moreover, excited electrons from the conduction band reacts easily with physiosorbed $O_{2(gas)}$ and it converts to $O^-_{2(hv)}$ via $e^- + O_{2(gas)} \rightarrow O^-_{2(hv)}$. This facilitates a quicker response and recovery to hydrogen gas via $O^-_{2(hv)} + H_2 \rightarrow H_2O + e^-$. The presence of Pd and PdO causes a reduction in the photoinduced electron–hole recombination.

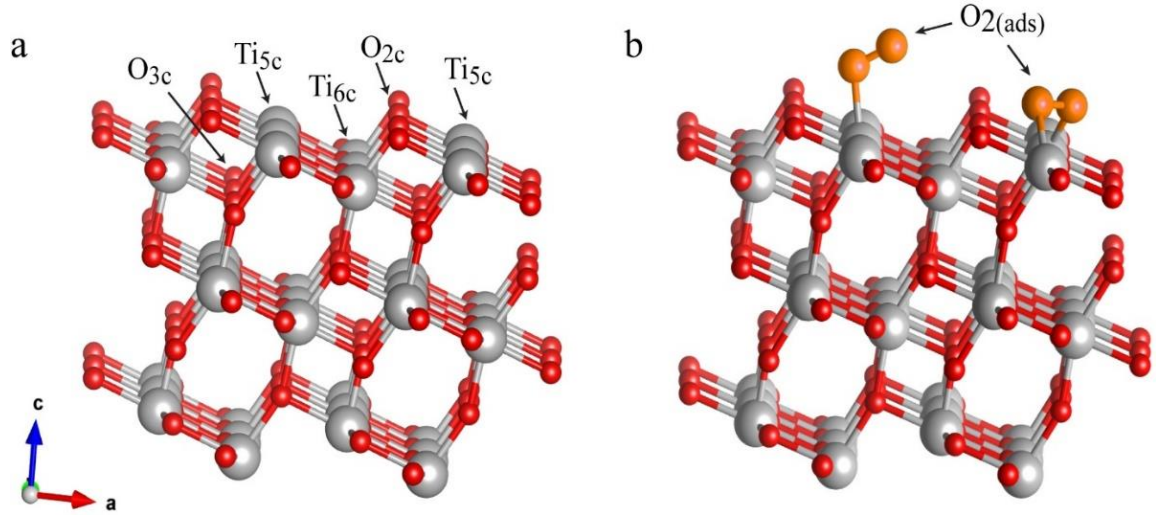


**Figure 10.** (**a**) Side view of (101) $TiO_2$ anatase phase and (**b**) oxygen adsorption sites on the (101) $TiO_2$ anatase phase.

Furthermore, the presence of the metallic Pd involves in the enhancement of hydrogen sensing performances by participating as a chemical sensitization agent via collecting hydrogen as a $Pd + \frac{x}{2}H_2 \rightarrow PdH_x$. Then, the collected hydrogen reacts with physiosorbed oxygen via $2PdH_x + \frac{x}{2}O^-_{2(hv)} \rightarrow 2Pd + xH_2O + xe^-$, forming water molecules and metallic Pd as a catalyst. Moreover, PdO also acts as a hydrogen collector when exposed to the hydrogen atmosphere as $PdO + H_2 \rightarrow Pd + H_2O$. Due to the reaction of Pd, PdO and $O^-_{2(hv)}$ with hydrogen, electrons are released, leading to a significant increase in the sensor current.

## 4. Conclusions

We have successfully synthesized Pd (nano-Schottky junctions)- and PdO (p–n heterojunctions)-incorporated $TiO_2$ NSs (HPT NSs) for hydrogen gas sensing in the range of 50–750 ppm at 30 °C under 565 nm light condition and 500 mV bias in the presence of humid conditions. The 565 nm visible light enables us to lower the response and recovery times (77/470 s) while maintaining the baseline. Furthermore, the lowest hydrogen concentration of 2 ppm is calculated theoretically at 30 °C under 565 nm light condition with 500 mV bias. In the sensing mechanism, Pd and PdO play an important role in hydrogen sensing via the formation of nano-Schottky junctions and p–n heterojunctions. In addition, Pd participates in the enhancement of the photoactivity of $TiO_2$ NSs. The highly selective HPT NSs provide a new pathway for hydrogen gas sensing under visible light conditions at low temperatures, with the advantage of requiring a low voltage bias.

**Author Contributions:** T.T.: Conceptualization, material synthesis, investigation, device fabrication, characterization, results analysis and writing of the original draft. C.J.H.: Assisting in data collection and data interpretation. R.K.H. and M.S.: Results analysis, reviewing and finalizing the draft, supervising, funding and managing the entire project. All authors have read and agreed to the published version of the manuscript.

**Funding:** This project received funding from the Australian Renewable Energy Agency (ARENA) as part of ARENA's Research and Development Program—Renewable Hydrogen for Export (Contract No. 2018/RND012). In addition, the work has been supported by the Future Energy Exports CRC (www.fenex.org.au) (accessed on 14 July 2023) whose activities are funded by the Australian Government's Cooperative Research Center Program.

**Institutional Review Board Statement:** Not applicable.

**Data Availability Statement:** Not applicable.

**Acknowledgments:** This activity received funding from the Australian Renewable Energy Agency (ARENA) as part of ARENA's Research and Development Program—Renewable Hydrogen for Export (Contract No. 2018/RND012). The views expressed herein are not necessarily the views of the Australian Government, and the Australian Government does not accept responsibility for any information or advice contained herein. This research was also supported by using the Nectar Research Cloud, a collaborative Australian research platform supported by the NCRIS-funded Australian Research Data Commons (ARDC). The authors would like to thank Jamie Riches for assistance in obtaining TEM images at the Central Analytical Research Facility (CARF) at QUT. S.K.T. Thathsara acknowledges the PhD scholarships under the Swinburne University Postgraduate Research Award (SUPRA). The authors acknowledge De Ming Zu for assistance in obtaining XPS data at Swinburne.

**Conflicts of Interest:** The authors declare no conflict of interest.

## Abbreviations

| | |
|---|---|
| RT | Room Temperature |
| NSs | Nanospheres |
| NPs | Nanoparticles |
| PT NSs | Pd-decorated $TiO_2$ NSs |
| HPT NSs | Hydrothermally Treated Pd-decorated $TiO_2$ NSs |

## References


1. Caliendo, C.; Russo, P.; Ciambelli, P. Hydrogen safety, state of the art, perspectives, risk assessment, and engineering solutions. *Util. Hydrog. Sustain. Energy Fuels* **2021**, *3*, 433.
2. Hashtroudi, H.; Yu, A.; Juodkazis, S.; Shafiei, M. Ultra-sensitive photo-induced hydrogen gas sensor based on two-dimensional $CeO_2$-Pd-PDA/rGO heterojunction nanocomposite. *Nanomaterials* **2022**, *12*, 1628. [CrossRef] [PubMed]
3. Sharma, S.; Ghoshal, S.K. Hydrogen the future transportation fuel: From production to applications. *Renew. Sustain. Energy Rev.* **2015**, *43*, 1151–1158. [CrossRef]
4. Chen, K.H.; Niu, J.S.; Liu, W.C. Study of a new hydrogen gas sensor synthesized with a sputtered cerium oxide thin film and evaporated palladium nanoparticles. *IEEE Trans. Electron Devices* **2021**, *68*, 4077–4083. [CrossRef]
5. Wang, L.; Yu, Y.M.; Zhang, Y.Q.; Zhang, J.; Lu, N.; Liu, N. Hydrogen breath test to detect small intestinal bacterial overgrowth: A prevalence case–control study in autism. *Eur. Child Adolesc. Psychiatry* **2018**, *27*, 233–240. [CrossRef]
6. Liu, J.; Li, S.; Zhang, B.; Xiao, Y.; Gao, Y.; Yang, Q.; Wang, Y.; Lu, G. Ultrasensitive and low detection limit of nitrogen dioxide gas sensor based on flower-like ZnO hierarchical nanostructure modified by reduced graphene oxide. *Sens. Actuators B Chem.* **2017**, *249*, 715–724. [CrossRef]
7. Huang, B.; Tong, X.; Zhang, X.; Feng, Q.; Rumyantseva, M.N.; Prakash, J.; Li, X. MXene/NiO composites for chemiresistive-type room temperature formaldehyde sensor. *Chemosensors* **2023**, *11*, 258. [CrossRef]
8. Thathsara, S.; Harrison, C.; Hocking, R.; Shafiei, M. Photoactive semiconducting metal oxides: Hydrogen gas sensing mechanisms. *Int. J. Hydrogen Energy* **2022**, *47*, 18208–18227. [CrossRef]
9. Kumar, R.; Liu, X.; Zhang, J.; Kumar, M. Room-temperature gas sensors under photoactivation: From metal oxides to 2D materials. *Nano-Micro Lett.* **2020**, *12*, 1–37. [CrossRef]
10. Choo, T.F.; Saidin, N.U.; Kok, K.Y. Hydrogen sensing enhancement of zinc oxide nanorods via voltage biasing. *R. Soc. Open Sci.* **2018**, *5*, 172372. [CrossRef]
11. Geng, Q.; He, Z.; Chen, X.; Dai, W.; Wang, X. Gas sensing property of ZnO under visible light irradiation at room temperature. *Sens. Actuators B Chem.* **2013**, *188*, 293–297. [CrossRef]
12. Lupan, O.; Ursaki, V.; Chai, G.; Chow, L.; Emelchenko, G.A.; Tiginyanu, I.; Gruzintsev, A.N.; Redkin, A. Selective hydrogen gas nanosensor using individual ZnO nanowire with fast response at room temperature. *Sens. Actuators B Chem.* **2010**, *144*, 56–66. [CrossRef]
13. Fan, S.W.; Srivastava, A.K.; Dravid, V.P. UV-activated room-temperature gas sensing mechanism of polycrystalline ZnO. *Appl. Phys. Lett.* **2009**, *95*, 142106. [CrossRef]
14. Nikfarjam, A.; Salehifar, N. Improvement in gas-sensing properties of $TiO_2$ nanofiber sensor by UV irradiation. *Sens. Actuators B Chem.* **2015**, *211*, 146–156. [CrossRef]
15. Peng, X.; Wang, Z.; Huang, P.; Chen, X.; Fu, X.; Dai, W. Comparative study of two different $TiO_2$ film sensors on response to $H_2$ under UV light and room temperature. *Sensors* **2016**, *16*, 1249. [CrossRef] [PubMed]
16. Li, T.; Zeng, W.; Shi, D.; Hussain, S. UV-enhanced hydrogen sensor based on nanocone-assembled 3D $SnO_2$ at low temperature. *Mater. Lett.* **2015**, *161*, 648–651. [CrossRef]
17. Varghese, O.K.; Gong, D.; Paulose, M.; Ong, K.G.; Dickey, E.C.; Grimes, C.A. Extreme changes in the electrical resistance of titania nanotubes with hydrogen exposure. *Adv. Mater.* **2003**, *15*, 624–627. [CrossRef]
18. Jun, Y.K.; Kim, H.S.; Lee, J.H.; Hong, S.H. High $H_2$ sensing behavior of $TiO_2$ films formed by thermal oxidation. *Sens. Actuators B Chem.* **2005**, *107*, 264–270. [CrossRef]
19. Zhu, T.; Gao, S.P. The stability, electronic structure, and optical property of $TiO_2$ polymorphs. *J. Phys. Chem. C* **2014**, *118*, 11385–11396. [CrossRef]
20. Bai, J.; Zhou, B. Titanium dioxide nanomaterials for sensor applications. *Chem. Rev.* **2014**, *114*, 10131–10176. [CrossRef]
21. Luo, Y.; Zhang, C.; Zheng, B.; Geng, X.; Debliquy, M. Hydrogen sensors based on noble metal doped metal-oxide semiconductor: A review. *Int. J. Hydrogen Energy* **2017**, *42*, 20386–20397. [CrossRef]
22. Drmosh, Q.; Hendi, A.; Hossain, M.; Yamani, Z.; Moqbel, R.; Hezam, A.; Gondal, M. UV-activated gold decorated rGO/ZnO heterostructured nanocomposite sensor for efficient room temperature $H_2$ detection. *Sens. Actuators B Chem.* **2019**, *290*, 666–675. [CrossRef]
23. Mai, H.D.; Jeong, S.; Nguyen, T.K.; Youn, J.S.; Ahn, S.; Park, C.M.; Jeon, K.J. Pd nanocluster/monolayer $MoS_2$ heterojunctions for light-induced room-temperature hydrogen sensing. *ACS Appl. Mater. Interfaces* **2021**, *13*, 14644–14652. [CrossRef] [PubMed]
24. Zhang, B.; Yang, F.; Liu, H.; Yan, L.; Yang, W.; Xu, C.; Huang, S.; Li, Q.; Bao, W.; Liu, B. Assembling graphene-encapsulated Pd/$TiO_2$ nanosphere with hierarchical architecture for high-performance visible-light-assisted methanol electro-oxidation material. *Ind. Eng. Chem. Res.* **2019**, *58*, 19486–19494. [CrossRef]
25. Thathsara, T.; Meilak, J.; Sangchap, M.; Harrison, C.; Hocking, R.; Shafiei, M. Visible light active rGO nanosheet encapsulated Pd quantum-sized dots decorated $TiO_2$ nano-spheres for hydrogen gas sensing at low temperatures. *Int. J. Hydrogen Energy* **2023**. [CrossRef]
26. Chen, P.; Hu, J.; Yin, M.; Bai, W.; Chen, X.; Zhang, Y. $MoS_2$ nanoflowers decorated with Au nanoparticles for visible-light-enhanced gas sensing. *ACS Appl. Nano Mater.* **2021**, *4*, 5981–5991. [CrossRef]
27. Xiong, Y.; Chen, J.; Wiley, B.; Xia, Y.; Yin, Y.; Li, Z.Y. Size-dependence of surface plasmon resonance and oxidation for Pd nanocubes synthesized via a seed etching process. *Nano Lett.* **2005**, *5*, 1237–1242. [CrossRef]

28. Damkale, S.R.; Arbuj, S.S.; Umarji, G.G.; Rane, S.B.; Kale, B.B. Highly crystalline anatase $TiO_2$ nanocuboids as an efficient photocatalyst for hydrogen generation. *RSC Adv.* **2021**, *11*, 7587–7599. [CrossRef]
29. Johnston, S.K.; Bryant, T.A.; Strong, J.; Lazzarini, L.; Ibhadon, A.O.; Francesconi, M.G. Stabilization of $Pd_{3-x}In_{1+x}$ polymorphs with Pd-like crystal structure and their superior performance as catalysts for semi-hydrogenation of Alkynes. *Chem. Cat. Chem.* **2019**, *11*, 2909–2918.
30. Wang, Z.; Wang, K.; Wang, H.; Chen, X.; Dai, W.; Fu, X. The correlation between surface defects and the behavior of hydrogen adsorption over ZnO under UV light irradiation. *Catal. Sci. Technol.* **2018**, *8*, 3260–3277. [CrossRef]
31. Xu, H.; Zhang, L. Controllable one-pot synthesis and enhanced photocatalytic activity of mixed-phase $TiO_2$ nanocrystals with tunable brookite/rutile ratios. *J. Phys. Chem. C* **2009**, *113*, 1785–1790. [CrossRef]
32. Hardcastle, F. Raman spectroscopy of titania ($TiO_2$) nanotubular water-splitting catalysts. *J. Ark. Acad. Sci.* **2011**, *65*, 43–48.
33. Challagulla, S.; Tarafder, K.; Ganesan, R.; Roy, S. Structure sensitive photocatalytic reduction of nitroarenes over $TiO_2$. *Sci. Rep.* **2017**, *7*, 8783. [CrossRef] [PubMed]
34. Chen, X.; Liu, L.; Yu, P.Y.; Mao, S.S. Increasing solar absorption for photocatalysis with black hydrogenated titanium dioxide nanocrystals. *Science* **2011**, *331*, 746–750. [CrossRef] [PubMed]
35. Wu, Z.; Dong, F.; Zhao, W.; Wang, H.; Liu, Y.; Guan, B. The fabrication and characterization of novel carbon doped $TiO_2$ nanotubes, nanowires and nanorods with high visible light photocatalytic activity. *Nanotechnology* **2009**, *20*, 235701. [CrossRef]
36. Dhawale, D.S.; Gujar, T.P.; Lokhande, C.D. $TiO_2$ nanorods decorated with Pd nanoparticles for enhanced liquefied petroleum gas sensing performance. *Anal. Chem.* **2017**, *89*, 8531–8537. [CrossRef]
37. Wang, J.; Rao, P.; An, W.; Xu, J.; Men, Y. Boosting photocatalytic activity of Pd decorated $TiO_2$ nanocrystal with exposed (001) facets for selective alcohol oxidations. *Appl. Catal. B* **2016**, *195*, 141–148. [CrossRef]
38. Camposeco, R.; Castillo, S.; Mejía-Centeno, I.; Navarrete, J.; Marín, J. Characterization of physicochemical properties of Pd/$TiO_2$ nanostructured catalysts prepared by the photodeposition method. *Mater. Charact.* **2014**, *95*, 201–210. [CrossRef]
39. Voogt, E.; Mens, A.; Gijzeman, O.; Geus, J. XPS analysis of palladium oxide layers and particles. *Surf. Sci.* **1996**, *350*, 21–31. [CrossRef]
40. Alenezy, E.K.; Sabri, Y.M.; Kandjani, A.E.; Korcoban, D.; Abdul Haroon Rashid, S.S.A.; Ippolito, S.J.; Bhargava, S.K. Low-temperature hydrogen sensor: Enhanced performance enabled through photoactive Pd-decorated $TiO_2$ colloidal crystals. *ACS Sens.* **2020**, *5*, 3902–3914. [CrossRef]
41. Hashtroudi, H.; Kumar, R.; Savu, R.; Moshkalev, S.; Kawamura, G.; Matsuda, A.; Shafiei, M. Hydrogen gas sensing properties of microwave-assisted 2D Hybrid Pd/rGO: Effect of temperature, humidity and UV illumination. *Int. J. Hydrogen Energy* **2021**, *46*, 7653–7665. [CrossRef]
42. Kapoor, A.; Ritter, J.; Yang, R.T. An extended Langmuir model for adsorption of gas mixtures on heterogeneous surfaces. *Langmuir* **1990**, *6*, 660–664. [CrossRef]
43. Thathsara, S.; Cooray, A.T.; Ratnaweera, D.R.; Mudiyanselage, T.K. A novel tri-metal composite incorporated polyacrylamide hybrid material for the removal of arsenate, chromate and fluoride from aqueous media. *Environ. Technol. Innov.* **2019**, *14*, 100353. [CrossRef]
44. Kumar, M.; Kumar, R.; Rajamani, S.; Ranwa, S.; Fanetti, M.; Valant, M. Efficient room temperature hydrogen sensor based on UV-activated ZnO nano-network. *Nanotechnology* **2017**, *36*, 365502. [CrossRef] [PubMed]
45. Long, G.L.; Winefordner, J.D. Limit of detection. A closer look at the IUPAC definition. *Anal. Chem.* **1983**, *55*, 712A–724A.
46. Chen, Y.; Pei, Y.; Jiang, Z.; Shi, Z.; Xu, J.; Wu, D.; Xu, T.; Tian, Y.; Wang, X.; Li, X. Humidity sensing properties of the hydrothermally synthesized WS2-modified $SnO_2$ hybrid nanocomposite. *Appl. Surf. Sci.* **2018**, *447*, 325–330. [CrossRef]
47. Hashtroudi, H.; Yu, A.; Juodkazis, S.; Shafiei, M. Two-Dimensional $Dy_2O_3$-Pd-PDA/rGO Heterojunction Nanocomposite: Synergistic Effects of Hybridisation, UV Illumination and Relative Humidity on Hydrogen Gas Sensing. *Chemosensors* **2022**, *10*, 78. [CrossRef]
48. Choudhury, S.; Betty, C.; Bhattacharyya, K.; Saxena, V.; Bhattacharya, D. Nanostructured PdO thin film from Langmuir–Blodgett precursor for room-temperature $H_2$ gas sensing. *ACS Appl. Mater.* **2016**, *8*, 16997–17003. [CrossRef]
49. Gao, Z.; Wang, T.; Li, X.; Li, Q.; Zhang, X.; Cao, T.; Li, Y.; Zhang, L.; Guo, L.; Fu, Y. Pd-decorated PdO hollow shells: A $H_2$-sensing system in which catalyst nanoparticle and semiconductor support are interconvertible. *ACS Appl. Mater.* **2020**, *12*, 42971–42981. [CrossRef]
50. Nguyen, T.T.; Van Dao, D.; Ha, N.T.T.; Van Tran, T.; Kim, D.-S.; Yoon, J.W.; Ha, N.N.; Lee, I.H.; Yu, Y.T. Superhigh sensing response and selectivity for hydrogen gas using PdPt@ ZnO core-shell nanoparticles: Unique effect of alloyed ingredient from experimental and theoretical investigations. *Sens. Actuators B Chem.* **2022**, *354*, 131083. [CrossRef]
51. Wang, D.; Yang, J.; Bao, L.; Cheng, Y.; Tian, L.; Ma, Q.; Xu, J.; Li, H.J.; Wang, X. Pd nanocrystal sensitization two-dimension porous $TiO_2$ for instantaneous and high efficient $H_2$ detection. *J. Colloid Interface Sci.* **2021**, *597*, 29–38. [CrossRef] [PubMed]
52. Geng, X.; Luo, Y.; Zheng, B.; Zhang, C. Photon assisted room-temperature hydrogen sensors using PdO loaded $WO_3$ nanohybrids. *Int. J. Hydrogen Energy* **2017**, *42*, 6425–6434. [CrossRef]
53. Li, Y.F.; Aschauer, U.; Chen, J.; Selloni, A. Adsorption and reactions of $O_2$ on anatase $TiO_2$. *Acc. Chem. Res.* **2014**, *47*, 3361–3368. [CrossRef]

54. Zeng, W.; Liu, T.; Wang, Z.; Tsukimoto, S.; Saito, M.; Ikuhara, Y. Oxygen adsorption on anatase $TiO_2$ (101) and (001) surfaces from first principles. *Mater. Trans.* **2010**, *51*, 171–175. [CrossRef]
55. Zhou, W.; Guan, Y.; Wang, D.; Zhang, X.; Liu, D.; Jiang, H.; Wang, J.; Liu, X.; Liu, H.; Chen, S. PdO/$TiO_2$ and Pd/$TiO_2$ heterostructured nanobelts with enhanced photocatalytic activity. *Chem. Asian J.* **2014**, *9*, 1648–1654. [CrossRef]